Electronic Supplementary Material (ESI) for Dalton Transactions.

Supporting Information

N-, S-atoms-coordinated Co_9S_8 trinary dopants within a porous graphene framework as efficient catalysts for oxygen reduction/evolution reactions

Yi Li, [1] Yazhou Zhou, [1, 2] Hejing Wen, [1] Juan Yang, *[1, 2] Chanez Maouche, [1] Qinqin Liu, [1, 2] Yunyan Wu, [1] Chao Cheng, [1] Jia Zhu, [1, 3] Xiaonong Cheng[1]

[1]School of Materials Science and Engineering, Jiangsu University, Zhenjiang 212013, China

[2]Jiangsu Key Laboratory for Chemistry of Low-Dimensional Materials, School of Chemistry and Chemical Engineering, Huaiyin Normal University, Huaian 223300, China

[3]School of Environmental and Chemical Engineering, Jiangsu University of Science and Technology, Zhenjiang 212003, China

*Corresponding author e-mail address: yangjuan6347@ujs.edu.cn

Electrochemical evaluations

Electrode potentials conversion. Potentials measured versus Ag/AgCl electrode were converted to a reversible hydrogen electrode (RHE) scale based on the following formula [S1]:

$$E_{vs\,\mathrm{RHE}}=E_{vs\,\mathrm{Ag/AgCl}}+E^0_{\mathrm{Ag/AgCl}}+0.059\mathrm{pH}\ \text{(in volts)} \qquad (1)$$

Kouteky-Levich (K-L) plots. The working electrode was scanned cathodically at the rate of 10 mV s^{-1} with the rotation speed from 225 to 2500 rpm. The relevant K-L plots ($-J^{-1}$ *vs.* $\omega^{-1/2}$) are calculated by the following formula [S2]:

$$\frac{1}{J}=\frac{1}{J_k}+\frac{1}{J_d}=\frac{1}{J_k}+\frac{1}{B\omega^{1/2}} \qquad (2)$$

$$B=0.62nFC_0{D_0}^{2/3}\mu^{-1/6} \qquad (3)$$

where B and ω are the reciprocal of the slope and the angular velocity of the electrode, respectively, n is the transferred electrons for ORR, F is the Faraday constant (F=96485 C mol^{-1}), μ is the kinematic viscosity of the electrolyte (0.01 cm^2 s^{-1}), D_0 is the diffusion coefficient of O_2 in 0.1 M KOH (D_0=1.9×10^{-5} cm^2 s^{-1}), and C_0 is the concentration of O_2 (C_0=1.2×10^{-6} mol cm^{-3}). Furthermore, J_k is the kinetic-limiting current density, and J_d is the diffusing-limiting current density. The constant 0.62 is adopted when the rotation rate is expressed in rad s^{-1}. J_k can be calculated from J_d according to eq2 [S2]:

$$J_k = \frac{J \times J_d}{J_d - J} \tag{4}$$

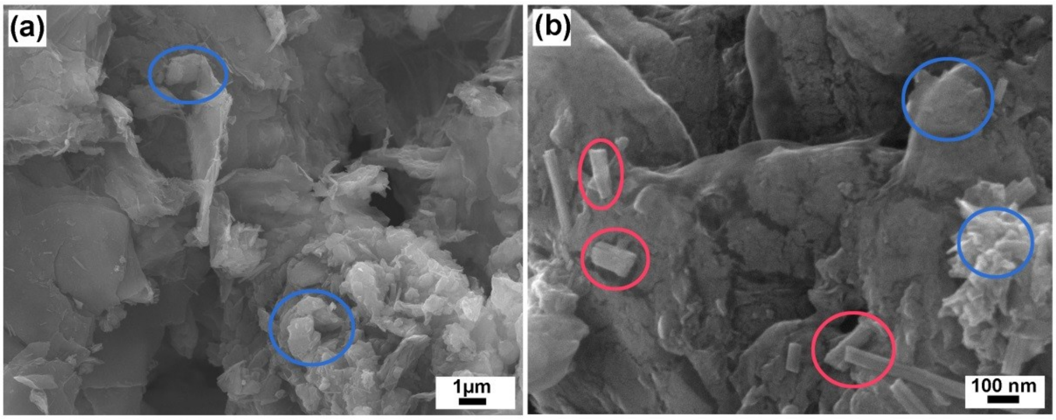

Fig. S1 SEM images (a, b) of MFR-bonded rGO.

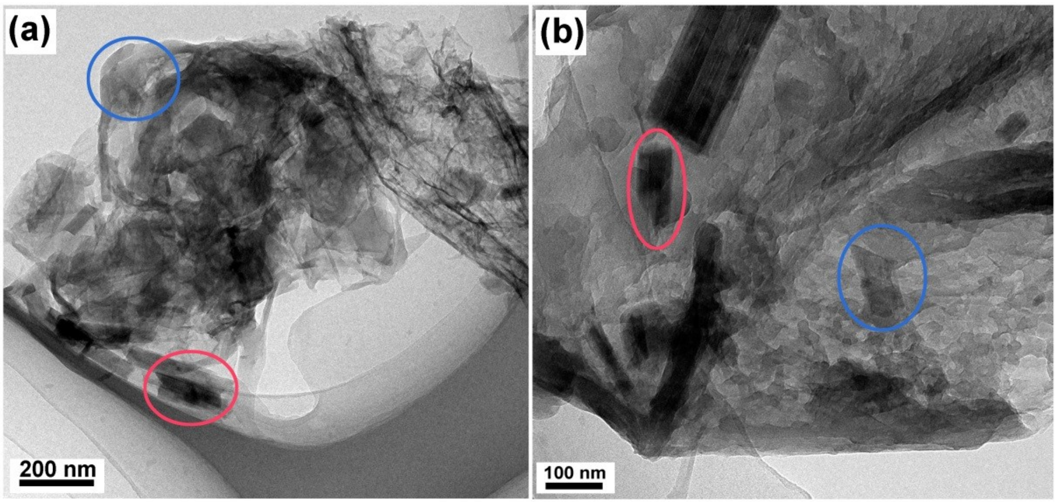

Fig. S2 TEM images (a, b) of MFR-bonded rGO.

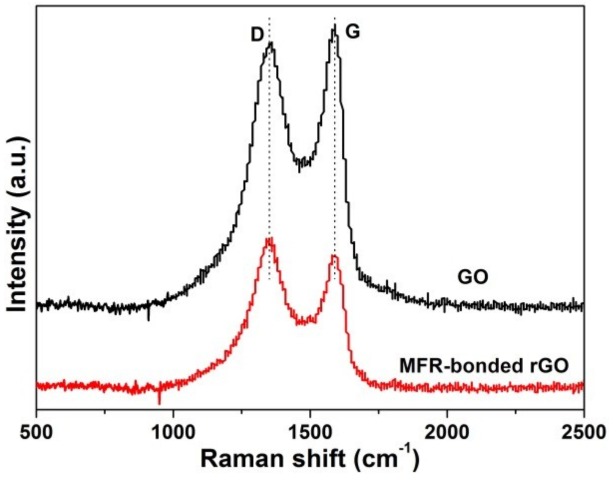

Fig. S3 Raman spectra of GO and MFR-bonded rGO.

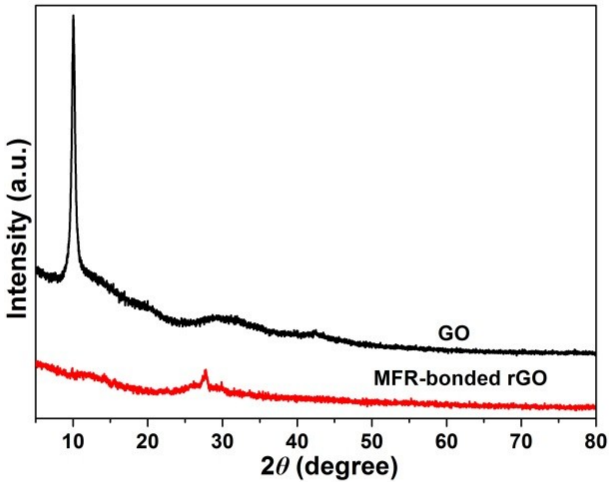

Fig. S4 XRD of GO and MFR-bonded rGO.

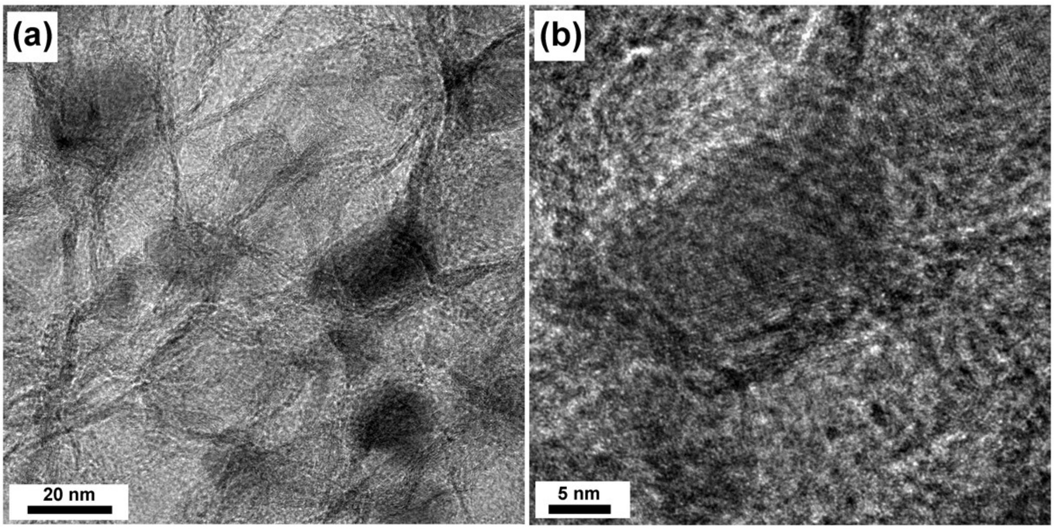

Fig. S5 HRTEM images of the Co_9S_8@NS-3DrGO-850.

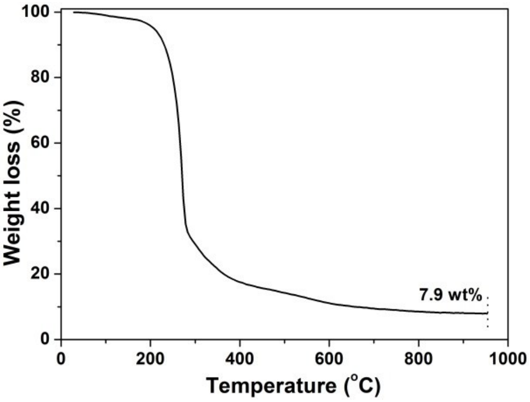

Fig. S6 Thermogravimetric analysis of the MFR-bonded mixture.

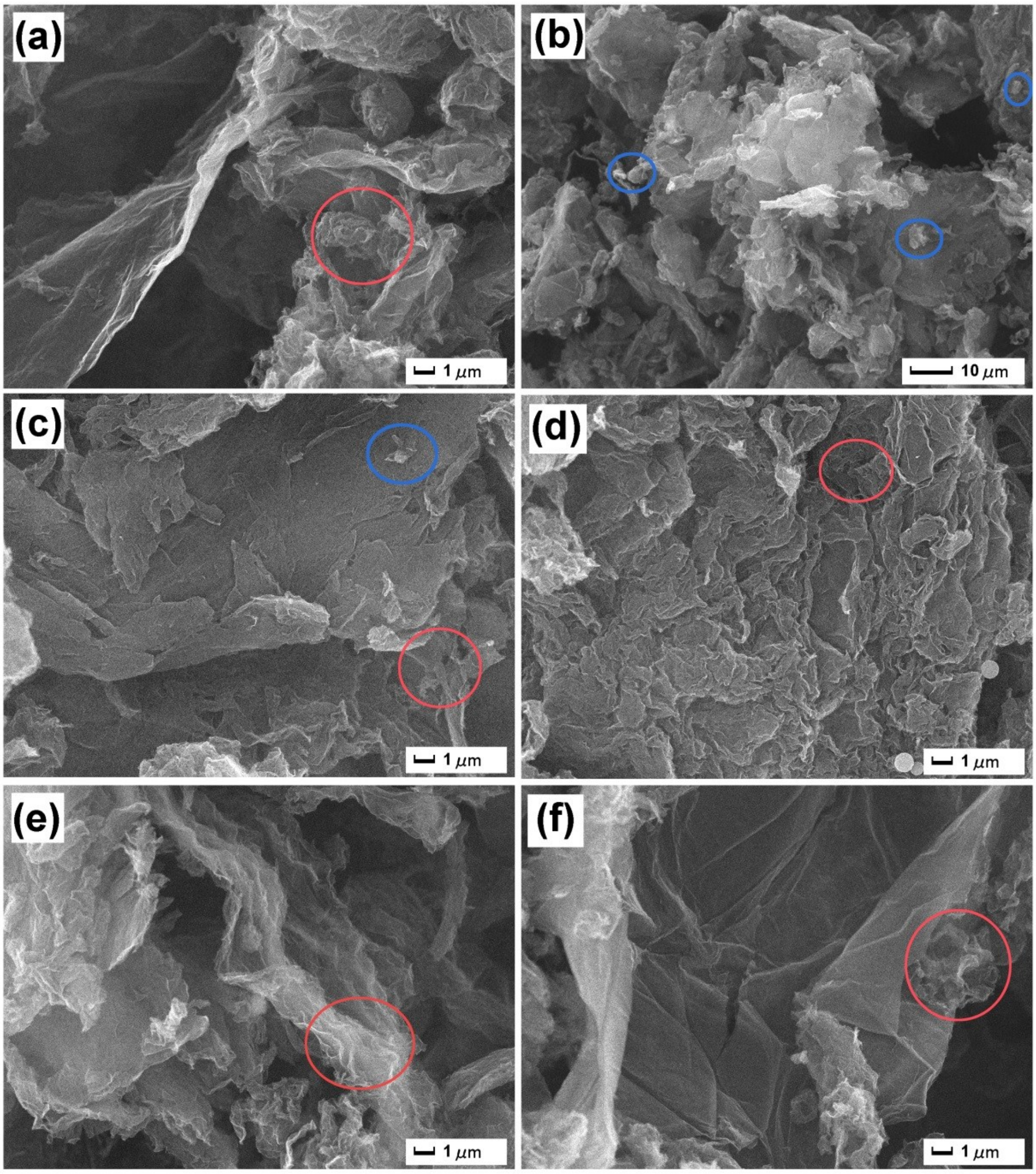

Fig. S7 SEM images for different products of the NS-3DrGO (a); Co_9S_8@NS-3DrGO-650 (b, c); Co_9S_8@NS-3DrGO-750 (d); Co_9S_8@NS-3DrGO-850 (e); and Co_9S_8@NS-3DrGO-950 (f), red circles highlight the porous structure, while blue circles highlight the MFR residues.

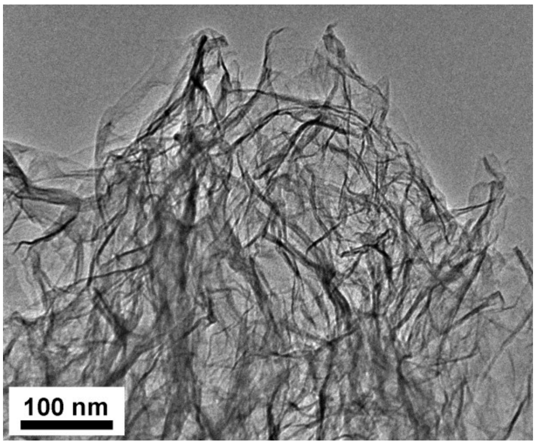

Fig. S8 TEM images of the NS-3DrGO.

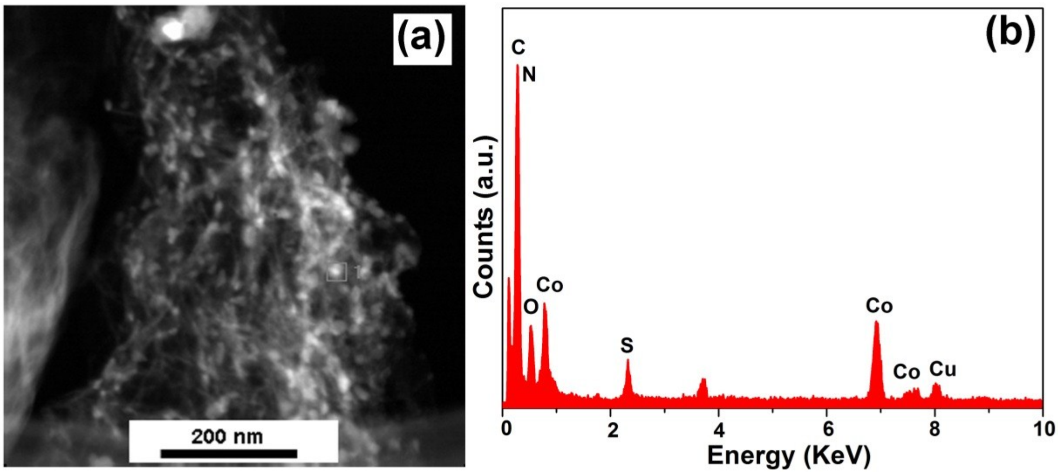

Fig. S9 The STEM image (a); and the EDS spectrum (b) of the Co_9S_8@NS-3DrGO-850 composite.

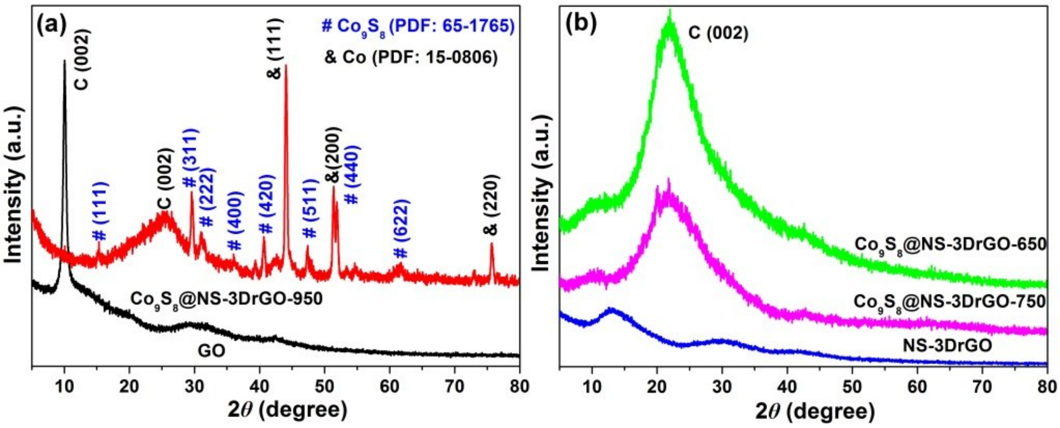

Fig. S10 The XRD patterns of (a) GO and Co_9S_8@NS-3DrGO-950; (b) NS-3DrGO, Co_9S_8@NS-3DrGO-650, and Co_9S_8@NS-3DrGO-750.

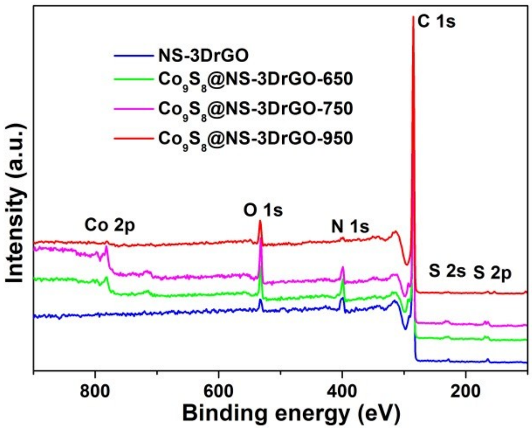

Fig. S11 XPS survey spectra of the NS-3DrGO and Co_9S_8@NS-3DrGO-*X* (*X*=650, 750, and 950).

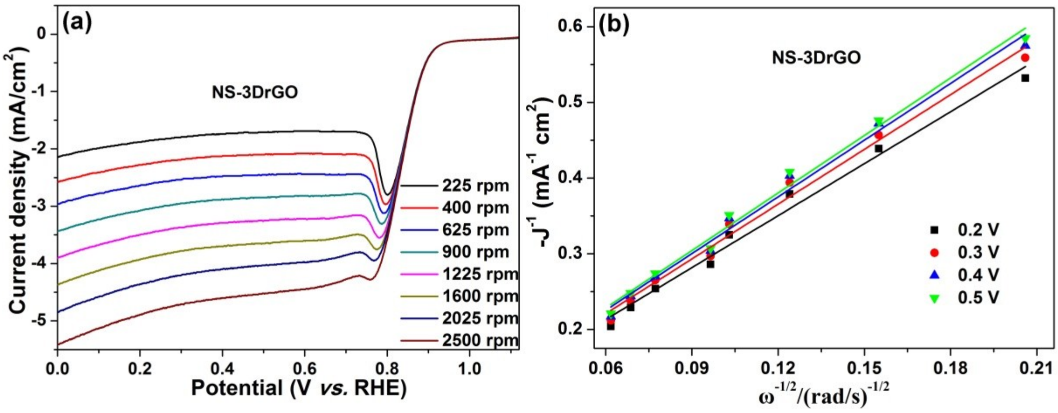

Fig. S12 (a) LSV curves of the NS-3DrGO at the rotating rate from 225 rpm to 2500 rpm; (b) is the corresponding K-L plots of current density reciprocal ($-J^{-1}$) versus $\omega^{-1/2}$ at different potentials.

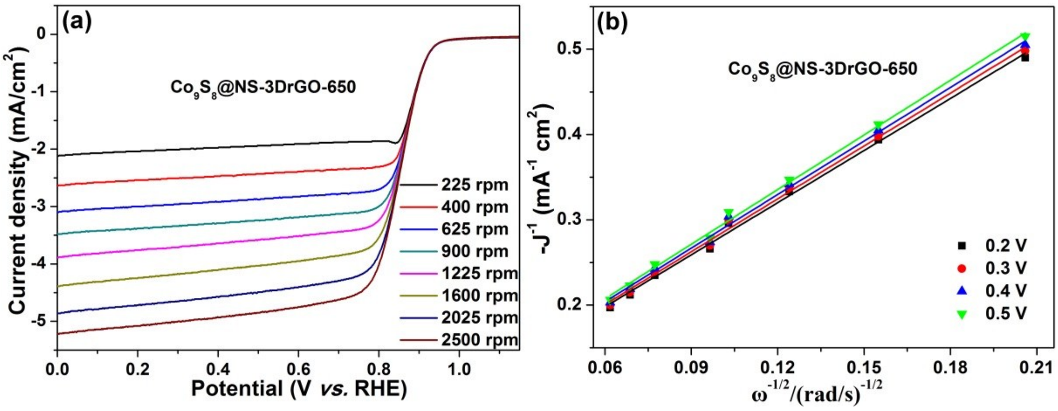

Fig. S13 (a) LSV curves of the Co_9S_8@NS-3DrGO-650 at the rotating rate from 225 rpm to 2500 rpm; (b) is the corresponding K-L plots of current density reciprocal ($-J^{-1}$) versus $\omega^{-1/2}$ at different potentials.

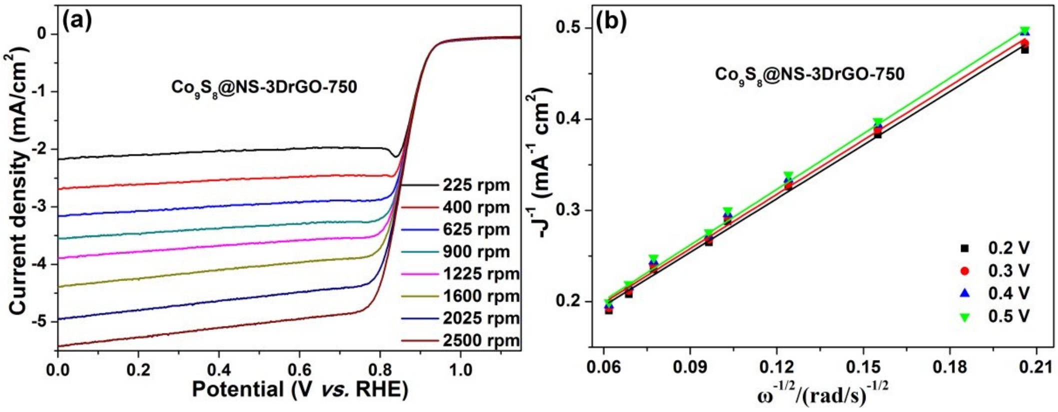

Fig. S14 (a) LSV curves of the Co_9S_8@NS-3DrGO-750 at the rotating rate from 225 rpm to 2500 rpm; (b) is the corresponding K-L plots of current density reciprocal ($-J^{-1}$) versus $\omega^{-1/2}$ at different potentials.

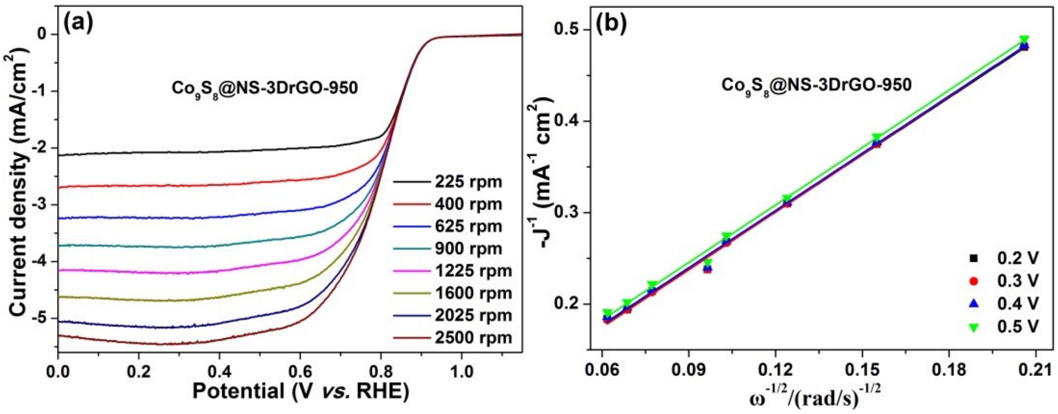

Fig. S15 (a) LSV curves of the Co$_9$S$_8$@NS-3DrGO-950 at the rotating rate from 225 rpm to 2500 rpm; (b) is the corresponding K-L plots of current density reciprocal ($-J^{-1}$) versus $\omega^{-1/2}$ at different potentials.

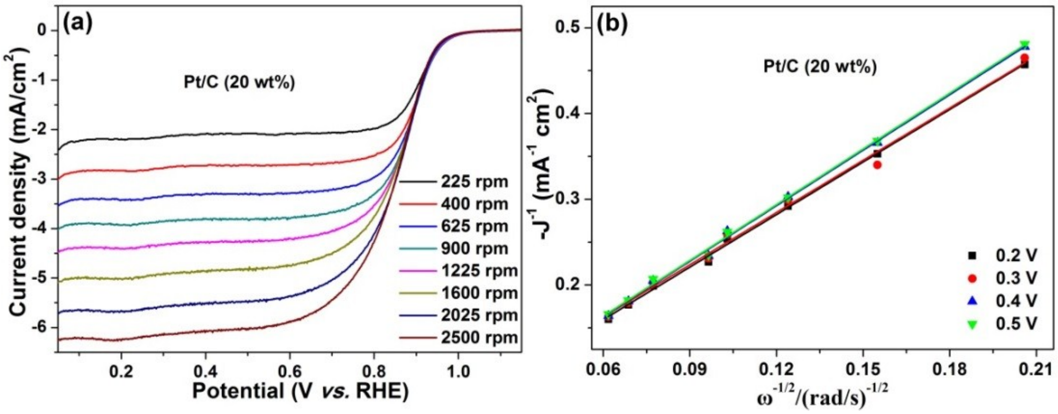

Fig. S16 (a) LSV curves of the Pt/C (20 wt%) at the rotating rate from 225 rpm to 2500 rpm; (b) is the corresponding K-L plots of current density reciprocal ($-J^{-1}$) versus $\omega^{-1/2}$ at different potentials.

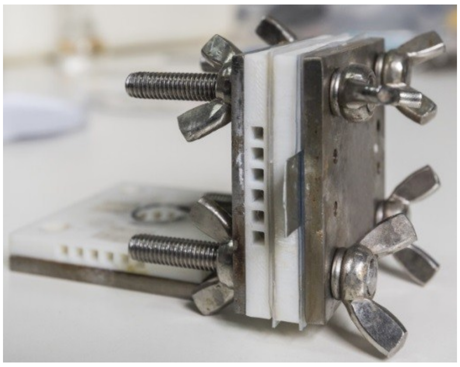

Fig. S16 Digital photo a home-made Zn-air battery.

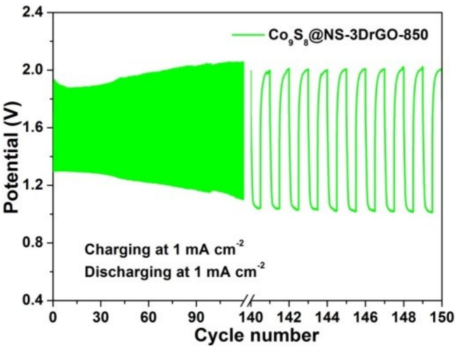

Fig. S17 Galvanostatic discharge and charge cycling stability of Zn-air battery using Co_9S_8@NS-3DrGO-850 at a current density of 1 mA cm^{-2} with each cycle being 300 s.

Table S1 ICP-AES analysis of the Co_9S_8@NS-3DrGO-650, Co_9S_8@NS-3DrGO-750, Co_9S_8@NS-3DrGO-850, and Co_9S_8@NS-3DrGO-950

Samples	**Cobalt composition (wt %)**
Co_9S_8@NS-3DrGO-650	6.27
Co_9S_8@NS-3DrGO-750	10.71
Co_9S_8@NS-3DrGO-850	11.84
Co_9S_8@NS-3DrGO-950	26.53

Table S2 The values of I_D/I_G for different composites, for comparison, the I_D/I_G value of GO and NS-3DrGO are also presented.

Samples	**I_D/I_G**
GO	0.94
NS-3DrGO	1.13
Co_9S_8@NS-3DrGO-650	1.13
Co_9S_8@NS-3DrGO-750	1.09
Co_9S_8@NS-3DrGO-850	1.08
Co_9S_8@NS-3DrGO-950	1.04

Table S3 The specific surface area, pore size and pore volume of the different products.

Samples	**BET surface area (m^2 g^{-1})**	**Pore size (nm)**	**Pore volume (cm^3 g^{-1})**
NS-3DrGO	402.5	38.0	0.529
Co_9S_8@NS-3DrGO-650	394.7	37.9	0.696
Co_9S_8@NS-3DrGO-750	351.9	37.9	0.662
Co_9S_8@NS-3DrGO-850	301.4	37.9	0.567
Co_9S_8@NS-3DrGO-950	176.7	106.8	0.319

Table S4 Electrochemical parameters extracted from LSV curves in Fig. 5b.

Samples	E_0 (V *vs.* RHE)	$E_{1/2}$ (V *vs.* RHE)	J_d at 0.2 V (mA cm^{-2})	$\bar{n}$
NS-3DrGO	0.869	0.794	-4.04	ca. 3.74
Co_9S_8@NS-3DrGO-650	0.897	0.816	-4.46	ca. 4.00
Co_9S_8@NS-3DrGO-750	0.888	0.817	-4.57	ca. 4.00
Co_9S_8@NS-3DrGO-850	0.951	0.826	-5.29	ca. 4.00
Co_9S_8@NS-3DrGO-950	0.855	0.758	-5.07	ca. 4.00
Pt/C	0.928	0.816	-5.04	ca. 4.00

Table S5 Electrochemical parameters extracted from LSV curves in Fig. 6a.

Samples	Onset potential at 1 mA cm^{-2} (V *vs.* RHE)	Overpotential at10 mA cm^{-2} (V *vs.* RHE)	*J* at 1.65 V (mA cm^{-2})	Tafel slope (mV dec^{-1})
NS-3DrGO	1.55	708	2.76	207
Co_9S_8@NS-3DrGO-650	1.56	470	7.54	108
Co_9S_8@NS-3DrGO-750	1.54	361	10.2	105
Co_9S_8@NS-3DrGO-850	1.49	317	18.6	102
Co_9S_8@NS-3DrGO-950	1.52	371	9.13	140
RuO_2	1.51	330	14.2	98

Table S6 The bifunctional activity of different catalysts for OER and ORR.

Samples	E_{ORR}/V at -3 mA cm^{-2}	E_{OER}/V at 10 mA cm^{-2}	ΔE/V (E_{J10}-E_{J-3})
NS-3DrGO	0.50	1.93	1.43
Co_9S_8@NS-3DrGO-850	0.83	1.73	0.90
RuO_2	0.23	1.82	1.59
Pt/C	0.80	1.95	1.15

Table S7 The bifunctional activity of different Co-based nanoparticles supported by carbons for OER and ORR.

Electrode materials	ΔE/V	Electrolyte (M KOH)	Catalyst loading (mg cm^{-2})	References
Co_9S_8(600)/N,S-GO	0.88	0.1	0.25	S1
Co_3O_4/N-rGO	0.93	0.1	0.13	S2
$CuCo_2O_4$/N-CNTs	0.90	0.1	0.20	S3

Co@Co_3O_4/NC-2	0.90	0.1	0.21	S4
Co_3O_4@PGC	1.02	0.1	0.20	S5
Co@N-PGCS	0.91	0.1	0.25	S6
NiCo/PFC	0.86	0.1	0.13	S7
Co_3O_4-NTO/N-rGO	0.93	1.0	0.15	S8
Co_9S_8@NS-3DrGO-850	0.90	0.1	0.20	This work

References:

[S1] P. Ganesan, M. Prabu, J. Sanetuntikul, S. Shanmugam, Cobalt sulfide nanoparticles grown on nitrogen and sulfur codoped graphene oxide: an efficient electrocatalyst for oxygen reduction and evolution reactions, *ACS Catal.* 2015, 5, 3625-3637.

[S2] Y. Li, C. Zhong, J. Liu, X. Zeng, S. Qu, X. Han, Y. Deng, W. Hu, J. Lu, Atomically thin mesoporous Co_3O_4 layers strongly coupled with N-rGO nanosheets as high-performance bifunctional catalysts for 1D knittable zinc–air batteries, *Adv. Mater.* 2017, 1703657.

[S3] H. Cheng, M. Li, C. Su, N. Li, Z. Liu, Cu-Co bimetallic oxide quantum dot decorated nitrogen-doped carbon nanotubes: a high-efficiency bifunctional oxygen electrode for Zn–air batteries, *Adv. Funct. Mater.* 2017, 27, 1701833.

[S4] A. Aijaz, J. Masa, C. Rçsler, W. Xia, P. Weide, A. J. R. Botz, R. A. Fischer, W. Schuhmann, M. Muhler, Co@Co_3O_4 encapsulated in carbon nanotube-grafted nitrogen-doped carbon polyhedra as an advanced bifunctional oxygen electrode, *Angew. Chem. Int. Ed.* 2016, 55, 4087-4091.

[S5] G. Li, X. Wang , J. Fu, J. Li, M. G. Park, Y. Zhang, G. Lui, Z. Chen, Pomegranate-inspired design of highly active and durable bifunctional electrocatalysts for rechargeable metal–air batteries, *Angew. Chem. Int. Ed.* 2016, 55, 4977-4982.

[S6] X. Liu, I. S. Amiinu, S. Liu, K. Cheng, S. Mu, Transition metal/nitrogen dual-doped mesoporous graphene-like carbon nanosheets for oxygen reduction and evolution reactions, *Nanoscale* 2016, 8, 13311-13320.

[S7] G. Fu, Y. Chen, Z. Cui, Y. Li, W. Zhou, S. Xin, Y. Tang, J. B. Goodenough, A novel hydrogel-derived bifunctional oxygen electrocatalyst for rechargeable air cathodes, *Nano Lett.* 2016, 16, 6516-6522.

[S8] X. Han, G. He, Y. He, J. Zhang, X. Zheng, L. Li, C. Zhong, W. Hu, Y. Deng, T. Ma,

Engineering catalytic active sites on cobalt oxide surface for enhanced oxygen electrocatalysis, *Adv. Energy Mater.* 2017, 1702222.